Electronic Supplementary Information

Tungsten Oxide Electron Transport Layer Enables Unprecedented Operational Stability in $MAPbI_3$ p-i-n Perovskite Solar Cells

Mohamed M. Elnaggar[a,b*], Lyubov A. Frolova[c], Ivan S. Zhidkov[d,e], Nikita A. Emelianov[c], Aleksandr S. Kramarenko[c], Xueqing Xu[f], Sergey M. Aldoshin[c], and Pavel A. Troshin[a,c*]

[a] Zhengzhou Research Institute of HIT, 26 Longyuan East 7th, Jinshui District, Zhengzhou, Henan Province, 450000, China

[b] Department of Physics, Faculty of Science, Tanta University, 31512 Tanta, Egypt

[c] Federal Research Center of Problems of Chemical Physics and Medicinal Chemistry, Russian Academy of Sciences (FRC PCP MC RAS), Semenov prospect 1, 141432 Chernogolovka, Moscow Region, Russian Federation

[d] Institute of Physics and Technology, Ural Federal University, Mira 19 Street,

Yekaterinburg, 620002, Russia

[e] M. N. Mikheev Institute of Metal Physics of Ural Branch of Russian Academy of Sciences,

S. Kovalevskoi 18 Street, Yekaterinburg, 620108, Russia

[f] Key Laboratory of Renewable Energy, Guangdong Provincial Key Laboratory of New and Renewable Energy Research and Development, Guangzhou Institute of Energy Conversion, Chinese Academy of Sciences, Guangzhou 510640, P.R. China

[*]Corresponding authors: elnaggar@hit.edu.cn, troshin2003@inbox.ru

Keywords: perovskite solar cells, tungsten oxide, electron transport layer, efficiency, interlayers, stability, ion diffusion blocking, device degradation.

Experimental procedures

Materials: PTAA had been purchased from Osilla. Lead (II) iodide (PbI_2, 99.999%), methylammonium iodide (MAI, >=99%) and [6,6]-phenyl-C_{61}-butyric acid methyl ester ($PC_{61}BM$) were purchased from FOMaterials (Russia). N,N-Dimethylformamide (DMF, >99.5%, anhydrous), N-Methyl-2-pyrrolidone (NMP, 98%, anhydrous), chlorobenzene (anhydrous, 99.9%, CB) and toluene (anhydrous, 99.5%), bathocuproine (BCP), 4,7-diphenyl-1,10-phenanthroline (BPhen) C_{60} and WO_3 (Nano powder) were purchased from Sigma-Aldrich.

Instrumental measurements

UV-VIS spectra of thin perovskite films were recorded using a two-channel fiber optic spectrometer Avantes AvaSpec-2048 with a two-dimensional matrix photodetector. Photoluminescence spectra were measured using an Ocean Optics OIQE-SET-02121 fiber optic spectrometer with a cooled high-sensitivity detector. XRD patterns of perovskite films and powders were collected using a Malvern PANalytical Aeris diffractometer with CuKα source at 20 ºC. FTIR spectra were obtained using Spectrum 100 Perkin Elmer FTIR spectrometer. The IR s-SNOM measurements were conducted in an inert atmosphere within a nitrogen-filled glove box by neaSNOM (Neaspec) in PsHet mode. VIT_P/Pt cantilevers (NT-MDT) with Pt tip coating, a probe radius of 25 – 35 nm, A typical resonance frequency of approximately 300 kHz and a force constant of 50 N/m were utilized for the measurements.

The X-ray photoelectron spectroscopy (XPS) spectra were measured on a PHI 5000 VersaProbe spectrometer (ULVAC-Physical Electronics, USA) with a spherical quartz monochromator and an energy analyzer operating in the energy range from 0 to 1500 eV. Electrostatic focusing with magnetic shielding makes it possible to obtain an energy resolution of $\Delta E < 0.5$ eV for Al Kα radiation (1486.6 eV). The analytical chamber was evacuated using

an ion pump. The XPS spectra were measured at a pressure of 10^{-7} Pa and calibrated on C 1s energy level of $MAPbI_3$ corresponding to C-H bond (285 eV).

Device fabrication:

ITO glass substrates were washed with deionized water, acetone, isopropanol for 10 min each in succession, and plasma treatment for 10 min at power 60. After that, all samples were transferred to the glovebox for deposition of functional layers. The PTAA (2.5 mg ml^{-1} in toluene) as hole transport material was spin-coated onto ITO (4000 rpm for 30 s), followed by an annealing at 100 °C for 10 min. Typically, the solution of perovskite consists of 1.45 M of PbI_2 and 1.4 M of MAI in the solvent mixture of 850 µl of DMF and 150 µl of NMP. $MAPbI_3$ solution (100 µL) was spun onto ITO/PTAA substrates at 4000 rpm for 40 s and then the films were quickly quenched with 160 µl toluene dripped 14 s after the start of the program. The films deposited were annealed at 80 °C for 5 min. The benchmark $PC_{61}BM$ ETL was spin-coated from solution (30 mg ml^{-1} in CB) at 3000 rpm for 30 s. For WO_X as ETL, it was deposited by thermal evaporation with different thickness (10, 20, 30, 60, and 90) in a high vacuum of ~1×10^{-5} mbar (rate ~ 0.1 - 0.5 Å s^{-1}). Also, C_{60} (10 nm), BCP (4 nm), and BPhen (4 nm) layers were deposited onto the $MAPbI_3$ films by thermal evaporation technique. Finally, Al (100 nm) top electrode was deposited by thermal evaporation through a shadow mask thus defining the device area of 0.08 cm^2.

Device characterization:

The J–V characteristics of the devices were measured inside MBraun glove box under nitrogen atmosphere using Advantest R6240A source-measurement unit and KHS Steuernagel solar simulator as a light source to simulate 100 mW cm^{-2} AM1.5G solar spectrum. The light flux was checked before and after the measurements using a calibrated silicon diode with a known spectral response. The experimental J_{SC} values were crosschecked with the values obtained by

integrating the EQE spectra against the standard AM1.5G spectrum. The EQE measurements were performed under ambient conditions for nonencapsulated devices. The EQE setup included 300 W Xenon lamp as a light source and automatic monochromator from LOMO instruments, Russia. The signal detection and processing were performed using SR510 lock-in amplifier combined with SR540 optical chopper (both from Stanford Research Instruments, USA).

Stability measurements

The device operational stability was investigated using a homemade setup integrated into MBraun glovebox. The illumination was provided by metal halide lamps (MHI800) with a spectrum similar to the solar AM1.5G spectrum. The light intensity was set at 100 mW cm^{-2}, and the temperature was maintained at 60 °C.

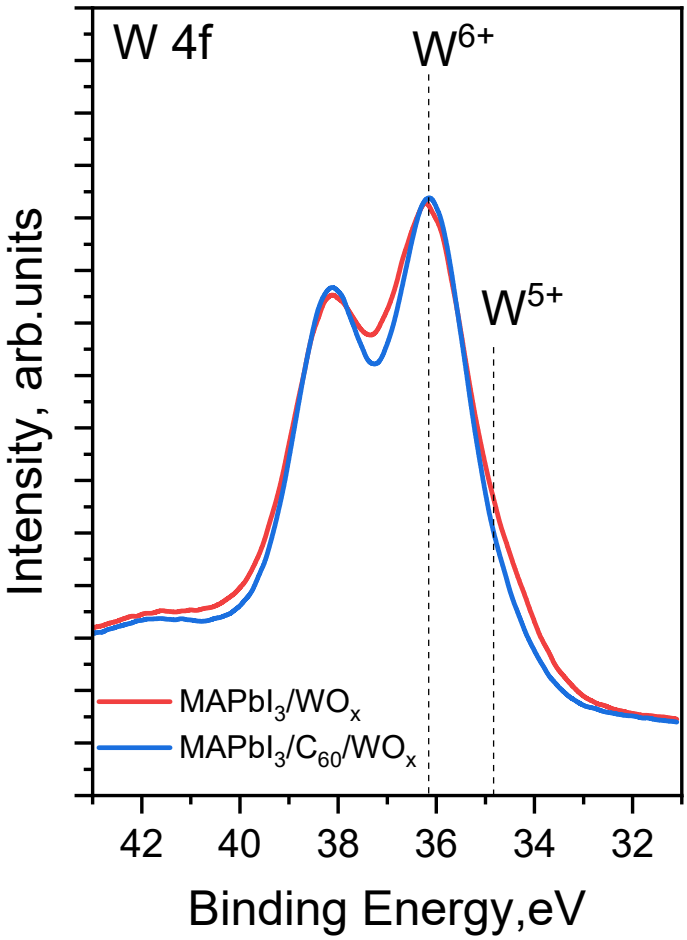

Figure S1. (a) XPS W 4f spectra of $MAPbI_3/WO_X$ and $MAPbI_3/C_{60}/WO_X$ films.

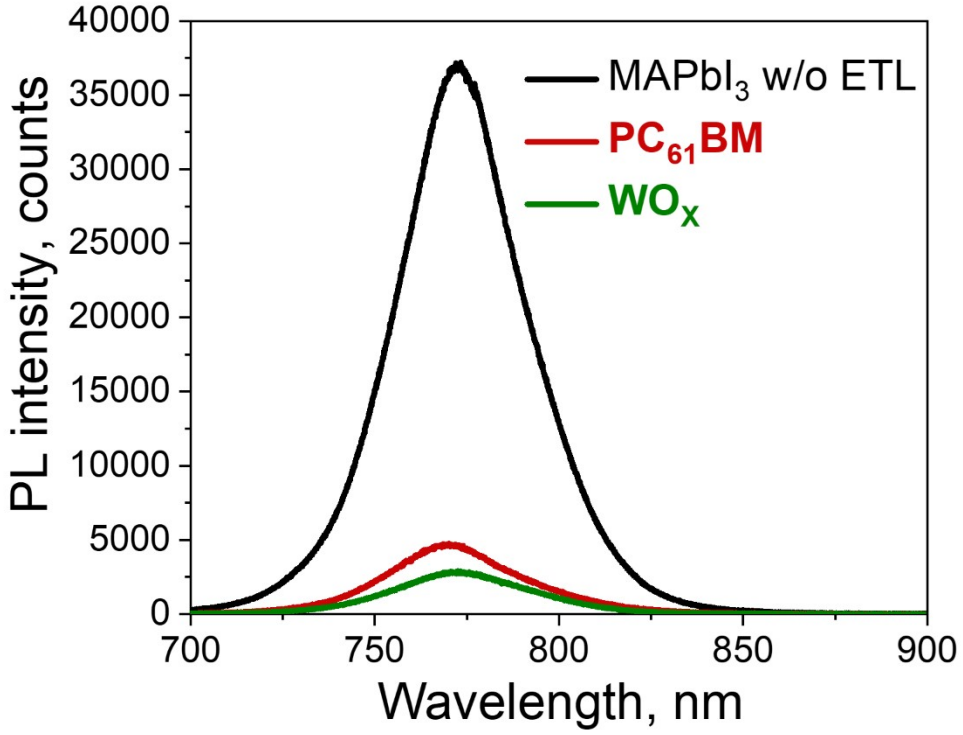

Figure S2. PL spectra of the glass/$MAPbI_3$, glass/$MAPbI_3$/$PC_{61}BM$, and glass/ $MAPbI_3$/WO_X samples.

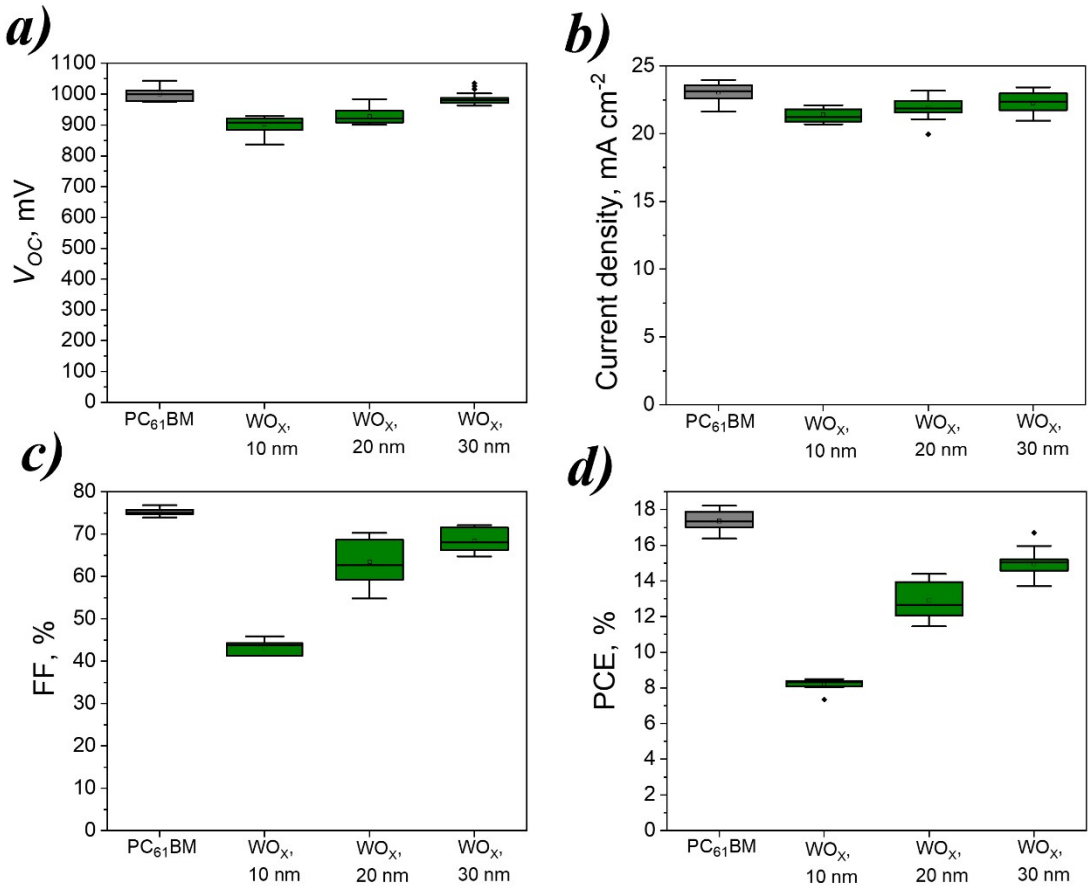

Figure S3. Statistics of device parameters for solar cells on ITO/PTAA $MAPbI_3/WO_X$/Al with different thickness of WO_X as single ETL compared to $PC_{61}BM$ as control.

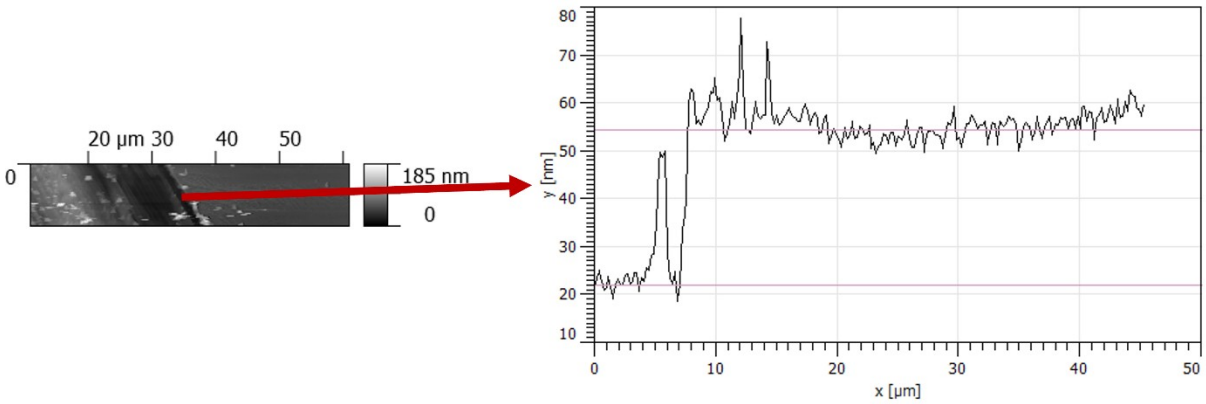

Figure S4. The AFM profile of the scratched WO_x film confirming that the real thickness is very close to the target value of 30 nm.

Table S1. Performance characteristics of p-i-n PSCs with different ETL composition.

ETL		V_{OC}, V	J_{SC}, mA cm^{-2}	FF, %	PCE, %
WO_X	**F**	1.025	22.4	65.7	15.1
	R	1.036	23.0	67.0	16.0
WO_x/BCP	**F**	0.992	22.7	64.0	14.4
	R	0.998	22.4	63.7	14.3
WO_x/Bphen	**F**	0.872	22.9	57.9	11.6
	R	0.985	22.8	57.3	12.9
C_{60}/WO_x	**F**	1.058	22.9	79.0	19.1
	R	1.080	23.2	76.6	19.2
C_{60}/WO_x/BCP	**F**	1.079	22.7	65.6	17.1
	R	1.069	23.0	70.2	17.3
C_{60}/WO_x/Bphen	**F**	1.089	22.3	66.0	16.0
	R	1.028	23.0	68.2	16.1
PCBM	**F**	1.086	23.0	76.1	19.0
	R	1.082	23.0	76.0	18.9
PCBM/WO_x	**F**	0.832	22.5	53.3	10.0
	R	0.824	22.7	50.6	9.5
PCBM/WO_x/BCP	**F**	0.960	20.6	45.2	8.9
	R	0.984	20.8	43.0	8.8
PCBM/WO_x/Bphen	**F**	0.911	22.1	25.9	5.2
	R	0.893	22.1	26.1	5.2

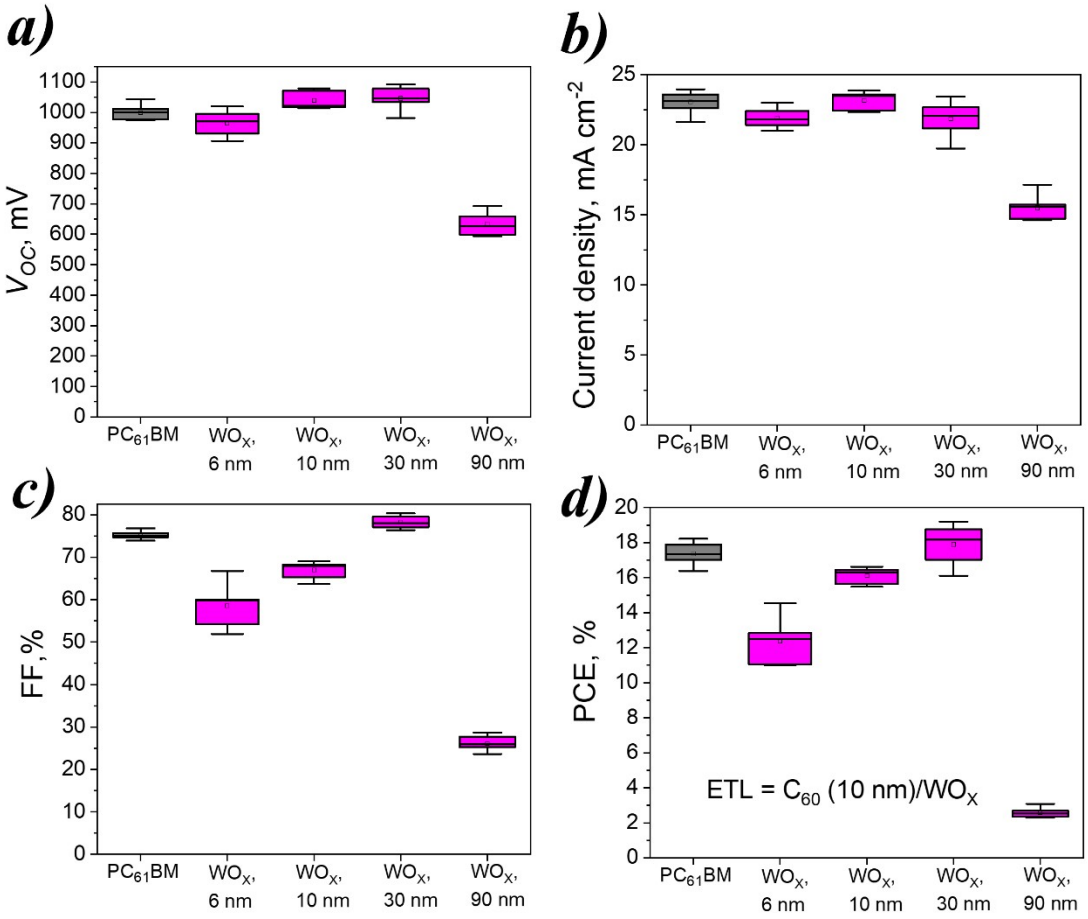

Figure S5. Statistics of device parameters for solar cells on ITO/PTAA/$MAPbI_3$/C_{60} (10 nm)/WO_X/Al with various thickness of WO_X.

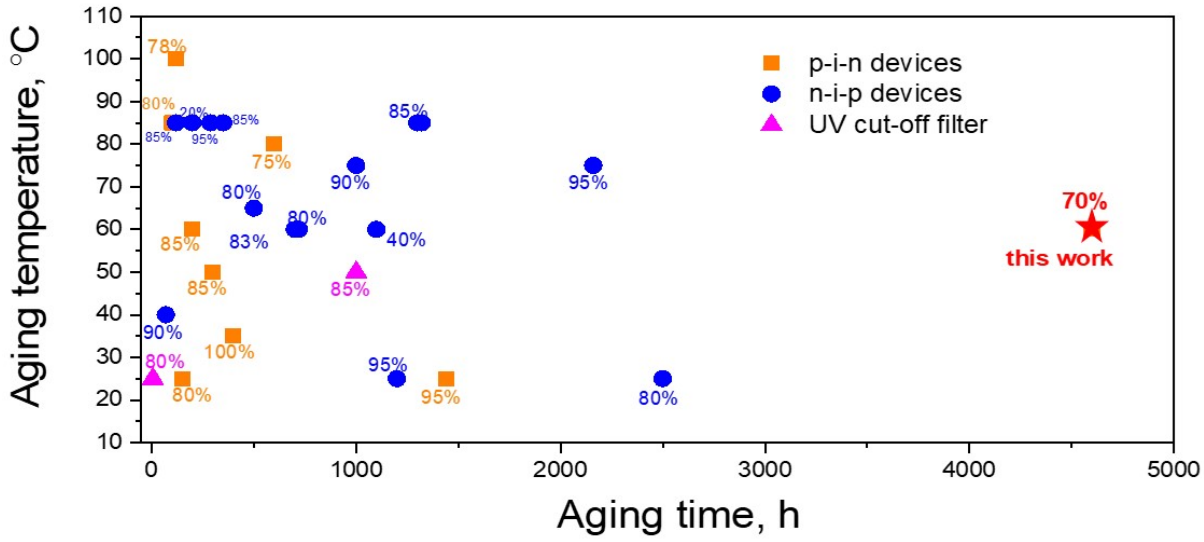

Figure S6. Comparative stability analysis of the operational stability of n-i-p and p-i-n $MAPbI_3$ perovskite solar cells under light illumination at different temperatures. This comparison highlights the remarkable stabilization effect of WO_X ETL.

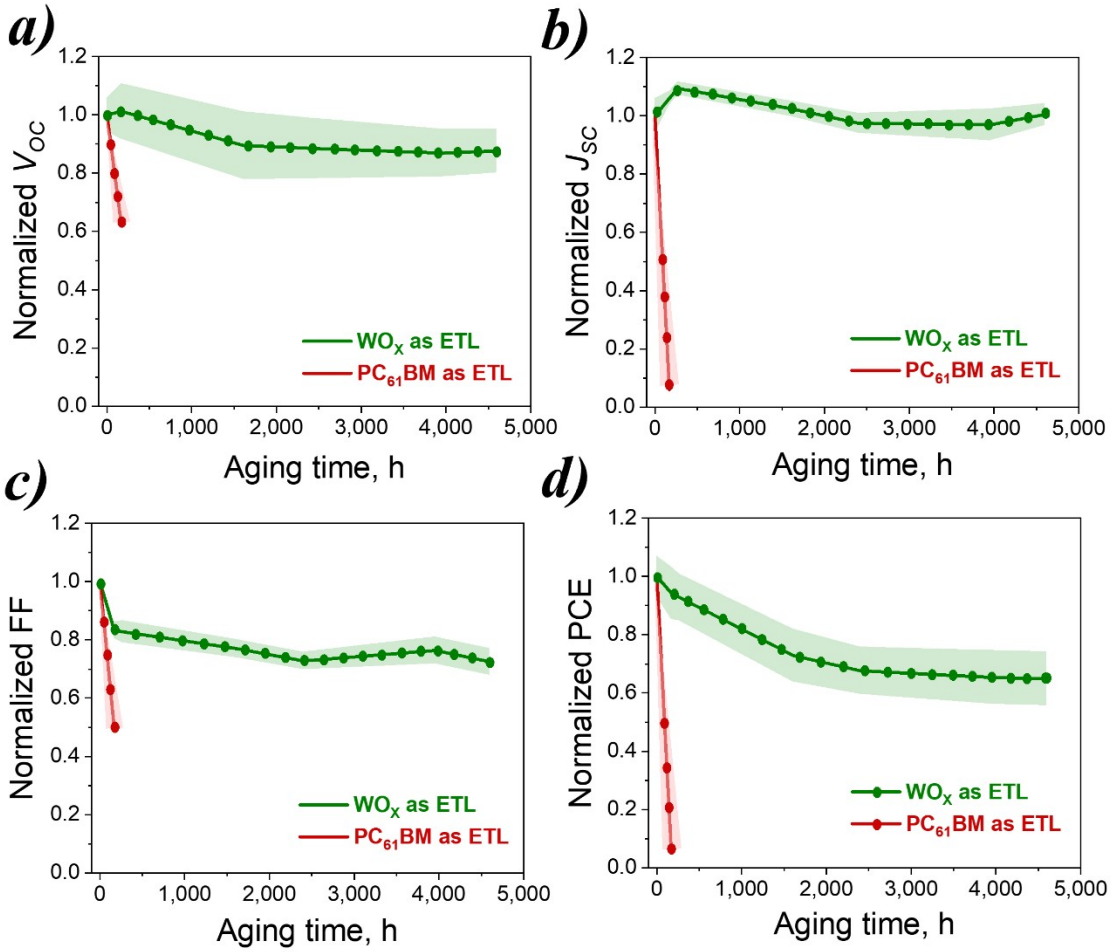

Figure S7. Evolution of the characteristics of ITO/PTAA/$MAPbI_3$/**ETL**/Al perovskite solar cells with WO_X and $PC_{61}BM$ as ETLs under continuous light soaking (60 °C, 100 mW cm^{-2}): open-circuit voltage (a), short-circuit current density (b), fill factor (c) and power conversion efficiency (d).

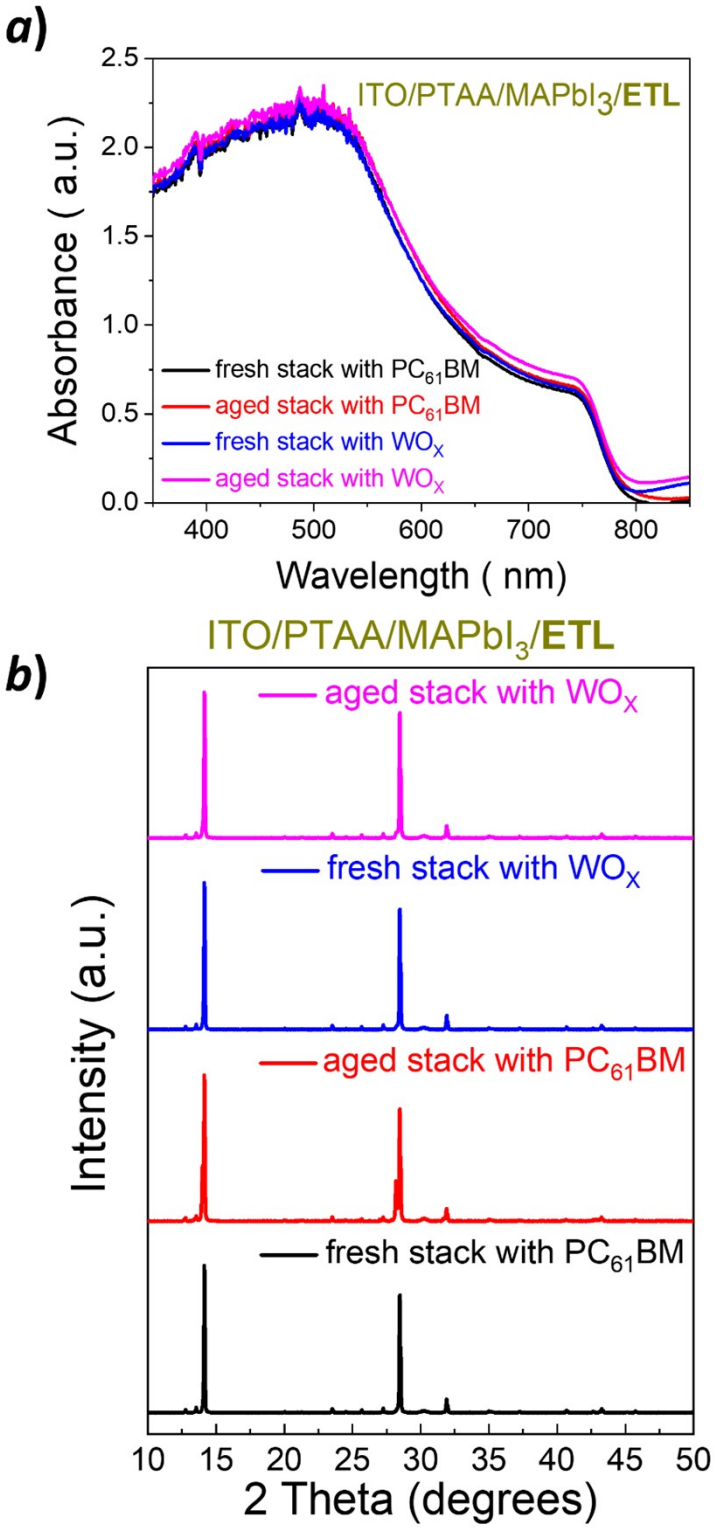

Figure S8. (a) UV-Vis absorption spectra performed on fresh and aged stacks using $PC_{61}BM$ and WO_X (30 nm) as top ETL coatings (100 h, 60 °C, 100 mW cm^{-2}), (b) XRD patterns of fresh and aged stacks under the same aging conditions.

DFT calculations

Density Functional Theory (DFT) calculations were performed within generalized gradient approximation with Perdew-Burke-Ernzerhof (PBE) functional[1] and spin-unrestricted formalism as implemented in CP2K program.[2,3] The core atomic levels were described with Goedecker-Teter-Hutter (GTH) type pseudopotentials[4], whereas double-zeta quality basis sets were used for the description of valence electrons. Long rage van der Waals interaction were taken into account by employing Grimme D3 correction.[5] Geometries of all studied structures were optimized until forces of 0.03 eV/Å were reached. Kinetic energy cutoff was set to 550 Ry, whereas the overall SCF accuracy was set to 10^{-8}. The electronic structure of WO_3 was described by DFT+U approach[6], applying an effective U_{eff} to the W-5d electrons. Figure S9 represents a linear fitting of the computed band gap dependence on the U_{eff} parameter.

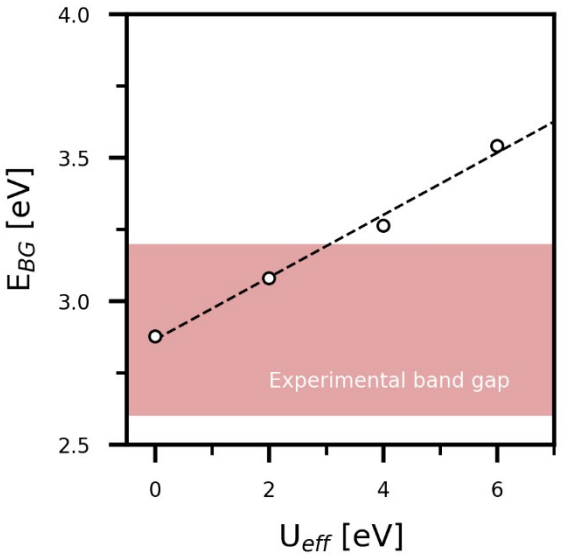

Figure S9. Dependence of the computed band gap energies (E_{BG}) on the U_{eff} term. Dashed line denotes linear fit to the computed values, whereas the red area represents range of experimentally measured band gaps. Cell optimizations of bulk WO_3 were performed for each U_{eff} value.

Our results show that U_{eff} of 2 eV can effectively reproduce experimental band gap, therefore, we utilized this value for further calculations of WO_x (100) surface and the interface. To prepare the surfaces of the $MAPbI_3$ and WO_x we firstly performed cell optimizations of the bulk $MAPbI_3$ and WO_3. $(CH_3NH_3)PbI_3$ ($MAPbI_3$) and WO_x (100) surfaces were used for slab calculations with a vacuum region added above the slab in order to separate periodic images along the direction perpendicular to the surface. All calculations were performed under the periodic boundary conditions.

For $MAPbI_3/WO_x$ interface preparations, we firstly pre-equilibrated interface using classical molecular dynamics (MD) simulations as implemented in CP2K software. As an initial step we constructed the interface by placing WO_x (100) surface over the $MAPbI_3$ (100) facet. $MAPbI_3$ atoms were fixed in all coordinates, whereas WO_3 atoms were completely relaxed. We performed MD simulation within the NVT ensemble at 1000 K for 1 ns. Later, the final geometry of the previous step was used as a starting geometry in NPT run at 1 atm and 300 K for 5 ns. Interactions between the atoms were modelled using Lennard-Jones potential using classical Lorentz-Berthelot combination rule. Force field parameters for MD simulation were taken from previously reported sources and summarized in Table S2.[7,8]

Table S2. Interatomic parameters for Lennard-Jones potential describing the interatomic interactions.

Atom type	**ε [eV]**	**σ [Å]**
Pb	0.00109	3.21
I	0.06389	4.01
C	0.00450	2.80
N	0.00185	3.79
H(C)	0.00412	1.54

H(N)	0.00151	2.04
W	0.00300	2.33
O	0.00778	3.12

Electrostatic charges of all atoms were taken from pure materials slabs calculations using RESP charges approach represented in CP2K for periodic systems.

For intramolecular parameters of the methyl ammonium cation, we used AMBER force field parameters as were suggested by Seijas-Bellido et al.[9] and summarized in the Table S3. Chemical bonds and molecular angles were described within the harmonic approximation.

Table S3. Bond parameters of methyl ammonium cations

Bond	**K [eV/Å^2]**	**R0 [Å]**
H(C) – C	29.3741	1.091
C – N	25.46276	1.499
H(N) – N	32.0019	1.033

Table S4. Angle parameters of methyl ammonium cations

Angle	**K [eV/rad^2]**	**Θ [deg]**
H(C) – C – N	4.250	107.9
H(C) – C – H(C)	3.382	110.7
H(N) – N – C	4.007	110.1
H(N) – N – H(N)	3.512	108.1

One torsion angle (H(C) – C – N – H(N)) was described using CHARMM like potential with the following force constant (K = 0.0067473 [eV]), multiplicity of the potential (M = 3) and phase of the potential (φ = 0 [deg])

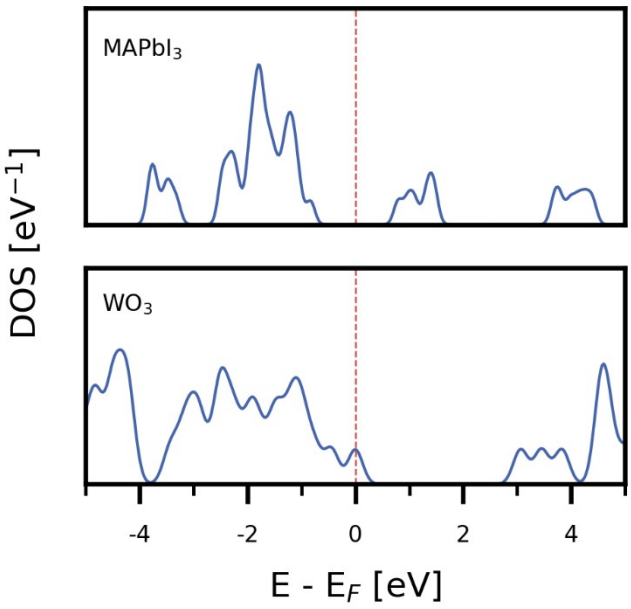

Figure S10. Total density of states of bulk $MAPbI_3$ and WO_3. Crimson line denotes the position if the Fermi level.

Surface energies and the interface formation energy can be computed using following expressions:

$$E_{SE} = \frac{E_{Surf.} - nE_{Bulk}}{2A}, \quad \text{(S1)}$$

where $E_{Surf.}$ is the final energy of the optimized surface, n is the number of atoms in the surface, E_{Bulk} is the energy of bulk material per atom and A is the surface area.

$$E_{IF} = \frac{E_{Interface} - n_{MAPbI_3} E^{bulk}_{MAPbI_3} - n_{WO_x} E^{bulk}_{WO_3}}{A} - E^{MAPbI_3}_{SE} - E^{WO_x}_{SE},$$

(S2)

where $E_{Interface}$ is the energy of the optimized interface structure, n_{MAPbI_3} is the number of atoms in $MAPbI_3$ part of the structure, n_{WO_x} is the number of atoms in WO_x part of the structure, $E^{bulk}_{MAPbI_3}$ is the energy per atom of bulk $MAPbI_3$, whereas $E^{bulk}_{WO_3}$ is the energy per atom of bulk WO_3, $E^{MAPbI_3}_{SE}$ is the surface energy of $MAPbI_3$ (100) surface and $E^{WO_x}_{SE}$ is the surface energy of amorphous WO_x surface.

Additional discussion of the computational results

Figure 5 of the main text summarizes our computational results of bulk materials, surfaces and the interface. Our findings show that in the $MAPbI_3$ (100) surface is the most favorable, showing negative surface energy of -0.98 J/m^2 (Equation S1), which can be related to the stabilization effect of the surface adsorbed methylammonium iodide (MAI).[10] Previous theoretical[11–17] and experimental[17–19] studies show that 100 facets are among the most stable surfaces for $MAPbI_3$ and WO_3, therefore, these initial structures were used for bare surfaces optimization. We checked representability of our surface models by direct comparison of the band gap (E_{BG}) and the work function (E_{WF}) values with the experimental values.

Work function of the material can be computed as the difference between the Fermi and vacuum energies. Thus, the computed E_{WF} of $MAPbI_3$ is 4.78 eV, which is close to the previously reported experimental E_{WF} of 4.70 eV[15]. At the same time, theoretically obtained E_{BG} from density of states distribution analysis of 1.88 eV is 0.28 – 0.38 eV larger than

experimentally measured band gap for $MAPbI_3$. For the bulk materials, positions of the Fermi levels were considered to be equal to the reversed values of the predicted E_{WF} of the corresponding surface. For the bulk $MAPbI_3$ we observed slight shrinkage of the band gap to 1.65 eV (Figure S2), which effectively reproduces experimental E_{BG} (experimental: 1.50 eV (this work), 1.55[11], 1.60[20]). Analyzing computational results of the bare WO_x (100) surface formation, we show that the surface energy of such facet is 0.33 J/m^2, whereas formation of amorphous WO_x surface is 0.70 J/m^2. As we can see from Figure 5 of the main text, formation of the surface significantly tightens the bulk WO_3 band gap from 3.07 eV (experimental: 3.1 eV (this work), 2.6 – 3.2[12], 3.26[21]) to almost 0.50 eV for the WO_x (100) facet and 1.67 eV for the amorphous WO_x. Theoretical work functions of these surfaces are 8.94 and 7.88 eV for the 100 and amorphous facets, which are far from the experimental E_{WF} for WO_3 (6.74 eV[21]), however, recent study of Sanchez et al.[22] showed the increase of the work function to 8.70 eV for the WO_x films obtained at 20 Pa. For the construction of the energy diagram (Figure 5 of the main text) we used experimentally obtained position of Fermi level (-6.74 eV). Now, we are moving to the description of the interface of $MAPbI_3/WO_x$ with the interface formation energy of 1.12 J/m^2 (Equation S2), whereas cohesive energy for such structure is also positive of 1.80 eV. Additionally, interface formation also decreases the BG width to 0.30 eV. This happens due to the intermediate electronic states. Figure S11 shows the projected density of states distribution of all studied structures.

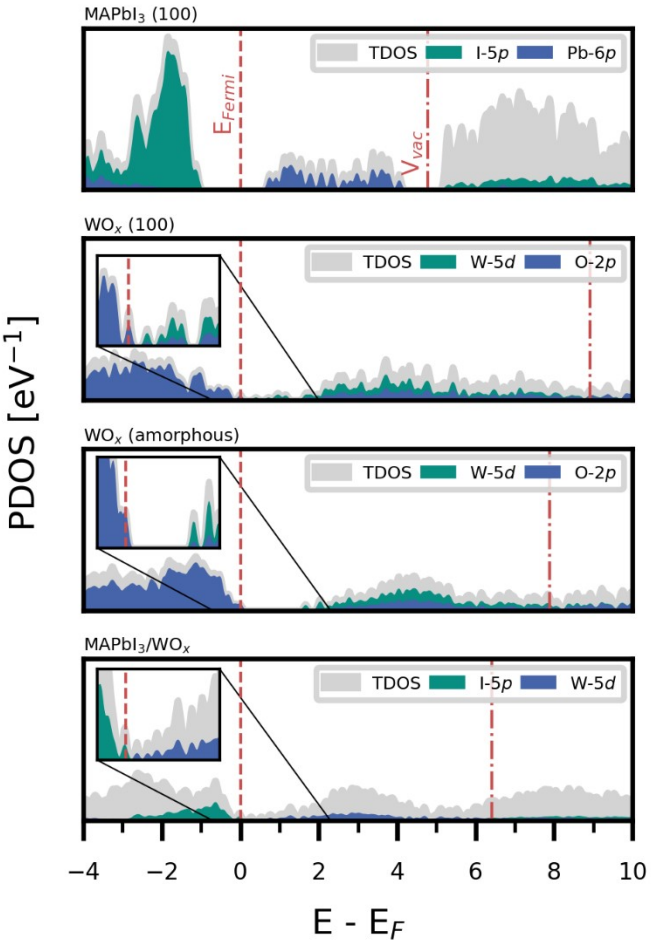

Figure S11. Representation of density of states of the studied structures. Dashed line represents the position of the Fermi level, whereas the chain line denotes the position of vacuum energy level.

It was shown that VMB of $MAPbI_3$ facets are formed mainly occupied by I-*2p* electrons, whereas the CMB are dominated by Pb-*6p* electrons. In the case of WO_x surfaces the band gap reduces to 0.54/1.67 eV (Figure S11), which are 2.53/1.40 eV smaller than the BG of bulk WO_3 and enhances electron transfer properties of this layer. The BG reduction proceeds through the formation of electronic states the Fermi level as shown in Figure S11, which are mainly coming from the W-*5d* electrons. These fluctuations are related to the formation of W^{5+} charge states at the surface.[23]

Finally, we discuss the interface structure analyzing the charge states of the surface atoms. Figure S12 represents the materials interplay together with the influence of the interface formation to the oxidation states of the atoms participating in the interface formation.

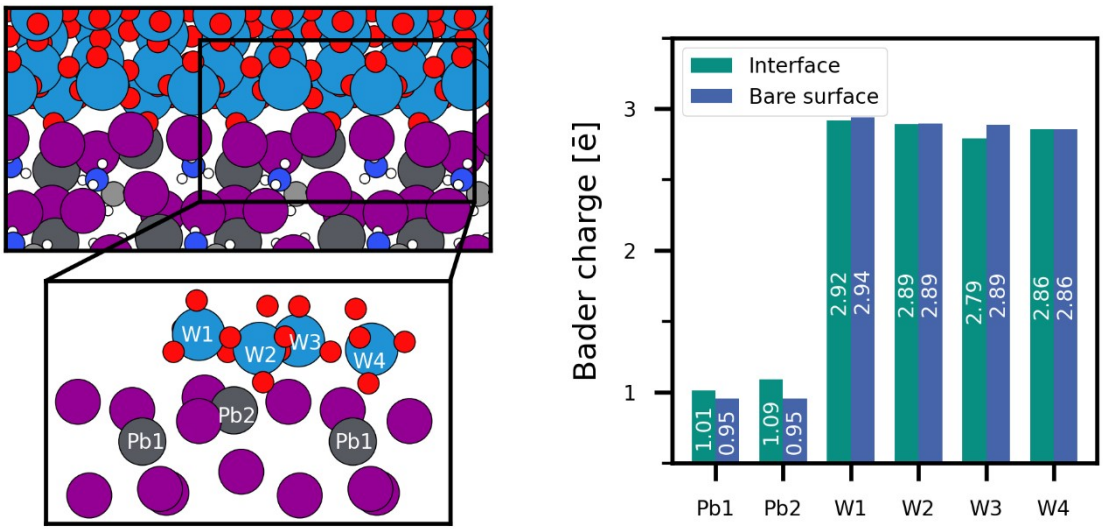

Figure S12. Representation of the interface between the $MAPbI_3$ and WO_x surfaces and the Bader charges (BC) of the surface Pb and W atoms. The red circles denote oxygen atoms, whereas the purple circles are iodine atoms.

We analyzed the oxidation states of the interfacial atoms and compared them with the oxidation states of the corresponding atoms at the bare surfaces. Figure S12 shows Bader charge (BC) analysis[24–27] that shows difference between the number of valence electrons and the computed number of electrons derived from the electron density and associated with the atoms. BC of the surface atoms of the bare surface stays unchanged (0.950e for $MAPbI_3$ (100) and 2.89e for WO_x (amorphous)) showing slight fluctuations. However, due to the interface formation Pb atoms loses more electrons showing BC of 1.01e (Pb1) and 1.09e (Pb2), determining more ionic pattern of the interface interactions, whereas for W the BC change is observed only for the W – I (W3) interacting tungsten atoms. Our findings show that the

$MAPbI_3/WO_x$ interface formation indeed stabilize the interfacial Pb^{2+} states, potentially suppressing their photolysis as was shown by the experiment.

References

1 J. P. Perdew, K. Burke and M. Ernzerhof, *Phys. Rev. Lett.*, 1996, **77**, 3865–3868.

2 T. D. Kühne, M. Iannuzzi, M. Del Ben, V. V. Rybkin, P. Seewald, F. Stein, T. Laino, R. Z. Khaliullin, O. Schütt, F. Schiffmann, D. Golze, J. Wilhelm, S. Chulkov, M. H. Bani-Hashemian, V. Weber, U. Borštnik, M. Taillefumier, A. S. Jakobovits, A. Lazzaro, H. Pabst, T. Müller, R. Schade, M. Guidon, S. Andermatt, N. Holmberg, G. K. Schenter, A. Hehn, A. Bussy, F. Belleflamme, G. Tabacchi, A. Glöß, M. Lass, I. Bethune, C. J. Mundy, C. Plessl, M. Watkins, J. VandeVondele, M. Krack and J. Hutter, *J. Chem. Phys.*, 2020, **152**, 194103.

3 J. Hutter, M. Iannuzzi, F. Schiffmann and J. VandeVondele, *WIREs Computational Molecular Science*, 2014, **4**, 15–25.

4 M. Krack, *Theor Chem Acc*, 2005, **114**, 145–152.

5 S. Grimme, S. Ehrlich and L. Goerigk, *Journal of Computational Chemistry*, 2011, **32**, 1456–1465.

6 Z. Hu and H. Metiu, *J. Phys. Chem. C*, 2011, **115**, 5841–5845.

7 X. Hao, J. Liu, M. Deng and Z. Fan, *J. Phys. Chem. C*, 2023, **127**, 20157–20168.

8 G. Duan, L. Chen, Z. Jing, P. De Luna, L. Wen, L. Zhang, L. Zhao, J. Xu, Z. Li, Z. Yang and R. Zhou, *Chem. Res. Toxicol.*, 2019, **32**, 1357–1366.

9 J. A. Seijas-Bellido, B. Samanta, K. Valadez-Villalobos, J. J. Gallardo, J. Navas, S. R. G. Balestra, R. M. Madero Castro, J. M. Vicent-Luna, S. Tao, M. C. Toroker and J. A. Anta, *J. Chem. Inf. Model.*, 2022, **62**, 6423–6435.

10 D. Meggiolaro, E. Mosconi, A. H. Proppe, R. Quintero-Bermudez, S. O. Kelley, E. H. Sargent and F. De Angelis, *ACS Energy Lett.*, 2019, **4**, 2181–2184.

11 E. E. Perry, J. G. Labram, N. R. Venkatesan, H. Nakayama and M. L. Chabinyc, *Advanced Electronic Materials*, 2018, **4**, 1800087.

12 F. Wang, C. Di Valentin and G. Pacchioni, *J. Phys. Chem. C*, 2011, **115**, 8345–8353.

13 E. Araujo-Lopez, M. Llano-Restrepo, J. Urresta-Aragon and J. A. Montoya, *Surface Science*, 2019, **681**, 149–157.

14 K. Zhang, Y. Li, Z. Fu, X. Chi, Y. Xiong, Y. Yao, X. Wang, Z. Tang, J. Wang, K. Nie, Z. Yang and Y.-M. Yan, *ACS Appl. Mater. Interfaces*, 2023, **15**, 15024–15035.

15 D. Kim, J.-H. Yun, M. Lyu, J. Kim, S. Lim, J. S. Yun, L. Wang and J. Seidel, *J. Phys. Chem. C*, 2019, **123**, 14144–14151.

16 J. Hu, G. Ji, X. Ma, H. He and C. Huang, *Applied Surface Science*, 2018, **440**, 35–41.

17 C. Ma, M.-C. Kang, S.-H. Lee, Y. Zhang, D.-H. Kang, W. Yang, P. Zhao, S.-W. Kim, S. J. Kwon, C.-W. Yang, Y. Yang and N.-G. Park, *J. Am. Chem. Soc.*, 2023, **145**, 24349–24357.

18 L. Jing, X. Cheng, Y. Yuan, S. Du, J. Ding, H. Sun, X. Zhan and T. Zhou, *J. Phys. Chem. C*, 2019, **123**, 10826–10830.

19 R. Lin, J. Wan, Y. Xiong, K. Wu, W. Cheong, G. Zhou, D. Wang, Q. Peng, C. Chen and Y. Li, *J. Am. Chem. Soc.*, 2018, **140**, 9078–9082.

20 M. Caputo, N. Cefarin, A. Radivo, N. Demitri, L. Gigli, J. R. Plaisier, M. Panighel, G. Di Santo, S. Moretti, A. Giglia, M. Polentarutti, F. De Angelis, E. Mosconi, P. Umari, M. Tormen and A. Goldoni, *Sci Rep*, 2019, **9**, 15159.

21 R. Hock, T. Mayer and W. Jaegermann, *J. Phys. Chem. C*, 2012, **116**, 18146–18154.

22 F. Sanchez, L. Marot, A. Dmitriev, R. Antunes, R. Steiner and E. Meyer, *Journal of Alloys and Compounds*, 2023, **968**, 171888.

23 C. Di Valentin, F. Wang and G. Pacchioni, *Top Catal*, 2013, **56**, 1404–1419.

24 E. Sanville, S. D. Kenny, R. Smith and G. Henkelman, *J Comput Chem*, 2007, **28**, 899–908.

25 M. Yu and D. R. Trinkle, *J. Chem. Phys.*, 2011, **134**, 064111.

26 W. Tang, E. Sanville and G. Henkelman, *J. Phys.: Condens. Matter*, 2009, **21**, 084204.

27 G. Henkelman, A. Arnaldsson and H. Jónsson, *Computational Materials Science*, 2006, **36**, 354–360.